1   TITLE (74 characters with spaces)

2   Indian Ocean Salinity build-up primes Deglacial Ocean Circulation Recovery

3

4   AUTHORS

5   Sophie Nuber*[1,2,3], James W. B. Rae[2], Xu Zhang[4], Morten B. Andersen[1], Matthew D.

6   Dumont[2], Huw T. Mithan[3], Yuchen Sun[5], Bas de Boer[6], Ian R. Hall[1], Stephen Barker[1]

7

8   AFFILIATIONS

9   [1]Cardiff University, [2]University of St. Andrews, [3]National Taiwan University, [4]Institute

10 of Tibet Plateau Research, Chinese Academy of Science, [5]Alfred Wegener Institute,

11 [6]Vrije Universiteit Amsterdam

12

13 ABSTRACT (162 words)

14 The Indian Ocean provides a source of salt for North Atlantic deep-water convection

15 sites, via the Agulhas Leakage (AL), and may thus drive changes in the ocean's

16 overturning circulation[6,7,8]. However, little is known about salt content variability of

17 Indian Ocean and AL waters during past glacial cycles, and how this may influence

18 circulation. Here we show that the glacial Indian Ocean surface salt budget was

19 notably different from the modern, responding dynamically to changes in sea level.

20 Indian Ocean surface salinity increases during glacial intensification peaking in glacial

21 maxima. We find that this is due to rapid land exposure in the Indonesian archipelago

22 induced by glacial sea level lowering, and we suggest a mechanistic link via reduced

23 input of relatively fresh Indonesian throughflow (ITF) waters into the Indian Ocean.

24 Using new climate model results, we show that the release of this glacial Indian Ocean

25 salinity via the Agulhas Leakage during deglaciation can directly impact the Atlantic

26 meridional overturning circulation and global climate.

27

28   Main (2510 words including subheadings)

29   The surface salinity distribution in the modern Indian Ocean differs from the

30   distribution patterns seen in the Atlantic and Pacific Oceans at comparable latitudes

31   (Figure 1). Tropical and subtropical Atlantic and Pacific surface waters are

32   characterised by their enhanced warmth and salinity. This is due to their re-circulation

33   in sunny subtropical gyres with high net-evaporation. The Indian Ocean is largely

34   located in the tropics and sub-tropics; however, modern Indian Ocean surface

35   conditions are notably fresher than comparable latitudes in the Atlantic and Pacific.

36   This is due to the inflow of monsoon-derived and Pacific-origin low salinity surface and

37   thermocline waters from the Indonesian Throughflow (ITF) (Figure 1). Inflow occurs

38   via the Timor, Lombok, and Ombai Straits[1], as well as the Bay of Bengal[2], and is

39   transported across the tropical Indian Ocean via the South Equatorial Current (SEC)[3,2,4].

40   Surface water salinity does increase within the subtropical western Indian Ocean[3], but

41   the salt is then partially exported through an active Agulhas Leakage[5]. The addition of

42   Indian Ocean salinity to Atlantic surface waters via the Agulhas Leakage has been

43   proposed as a mechanism to influence global ocean circulation by enhancing the

44   density potential at North Atlantic deep-water convection sites[6,7,8]. It is therefore

45   possible that changes in the ITF and subsequent Indian Ocean surface salinity could

46   impact global ocean circulation.

47   Here, we present coupled sea surface temperature (SST) from Mg/Ca in the planktonic

48   foraminifer *Globigerinoides ruber* (method after ref.[9]) and oxygen isotope-and SST-

49   based relative salinity reconstructions (method after ref.[10]) from western Indian

50   Ocean International Ocean Discovery Program Site U1476 located in the northern

51   entrance of the Mozambique Channel (15°49.25' S; 41°46.12' E; 2166 m) to investigate

52   changes in the western Indian Ocean surface hydrography. This site is strongly

53   influenced by the westward flowing SEC, with a minor contribution of recirculating

54   waters flowing directly from the southern Indian Ocean to Madagascar, and thus

55   tracks the hydrographic conditions of the tropical western Indian Ocean source waters

56   that feed into the Agulhas leakage[5]. Our 1.2 million year (Ma)-long record provides

57   the first evidence for changes in tropical western Indian Ocean hydrography beyond

58   the Last Glacial Maximum (LGM).

59

60   Glacial salinification and warming

61   Our data show that western Indian Ocean surface salinity and temperature structures

62   were significantly different from modern during Pleistocene glacial stages. ED Fig. 1

63   shows that western SEC temperature initially cools during glacial inception from its

64   interglacial high. However during the middle and latter phases of glacial cycles, this

65   cooling trend reverses and surface waters begin to warm. In the absence of other

66   influences, this warming would be expected to cause a decrease in planktic $\delta^{18}O$[11].

67   However, we find planktic $\delta^{18}O$ continues to increase, suggesting an increase in $\delta^{18}O_{sw}$

68   and hence surface salinity. Global growth in ice volume can only account for 50% of

69   the glacial-interglacial difference in $\delta^{18}O_{sw}$ throughout the last 1.2Ma (ED Fig. 2d). As

70   such, our data indicate a regional increase in sea surface salinity (as well as

71   temperature) during glacial periods. After correcting for the influence of global ice

72   volume changes (see Methods), our ice volume-corrected $\delta^{18}O_{sw}$ ($\delta^{18}O_{sw-ivc}$) and SST

73   data show average increases of 0.83‰ (±0.2‰ 2σ) and 4.4°C (±0.8°C 2σ), respectively

74   across 16 glacial cycles (ED Fig. 1). Glacial salinification occurs in 15 out of 16 glacial

75   cycles, with the onset of the glacial increase in $\delta^{18}O_{sw-ivc}$ occurring on average 20kyr

76   prior to the glacial termination in $\delta^{18}O_{benthic}$ (Figure 2a-d, ED Fig. 1, Methods). To

77   examine the regional consistency of this feature, we stacked SST and $\delta^{18}O_{sw-ivc}$ records

78   across the Indian Ocean (Figures 1 and 2) by resampling each record and averaging

79   the resulting records using a Gaussian smooth (ED Fig. 3; Methods). The resulting

80   Indian Ocean $\delta^{18}O_{sw-ivc}$ and SST stacks show the same patterns of salinification and

81   warming during intensification of glacial conditions (Figure 2a-d), suggesting this is an

82   Indian Ocean-wide phenomenon. The change in water mass properties does not apply

83   to Indian Ocean water source regions, such as the South China Sea (SCS) or the

84   western Pacific Ocean (ED Fig. 5; Methods). It is therefore likely to be connected to

85   dynamics in the Indian Ocean region.

86

87   Salinification not set up by atmosphere

88   Model simulations[12,13] and data reconstructions[14,15] show that Indian Ocean

89   temperature and salinity may be influenced by atmospheric circulation and monsoon

90   changes driven by precession. As such, we first examined precession-scale variability

91   within U1476 and stacked $\delta^{18}O_{sw-ivc}$ and SST using spectral analysis. We could not find

92   any significant precessional cycle in U1476 or in the stack, but we do identify a

93   significant 100 kyr periodicity in both, though note that caution is necessary when

94   interpreting the spectral analysis for the $\delta^{18}O_{sw-ivc}$ stack due to its coverage of only 345

95   kyr. (ED Fig. 6 and 7; Methods). This suggests that insolation-driven monsoonal

96   variability does not drive $\delta^{18}O_{sw-ivc}$ and SST in the western Indian Ocean, and only plays

97   a minor role for the whole tropical and subtropical Indian Ocean. The Bay of Bengal[14,15]

98   and Arabian Sea[16,17] have been highlighted as parts of the Indian Ocean where

99   monsoonal changes play a key role in surface ocean salinity changes which could

100   influence the subtropical Indian Ocean. However, $\delta^{18}O_{sw-ivc}$ records from both

101   locations also show 100 kyr periodicities within the last 1.2Ma (ED Fig. 8 and 9)

102   suggesting a glacial cycle overprint on Bay of Bengal and Arabian Sea surface salinity.

103   In fact, we find the same early salinification process in both the Bay of Bengal (ED Fig.

104   8) and Arabian Sea (ED Fig. 9 k-l) salinity reconstructions. This suggests that glacial

105   salinification is a ubiquitous feature of the Indian Ocean, and points towards a large-

106   scale mechanism that links changes in glacial ice volume to Indian Ocean surface

107   hydrography. Additionally, while some climate model simulations[12,13] suggest a

108   fresher glacial western Indian surface Ocean in line with a strengthened glacial Indian

109   Ocean dipole compared to modern, our data indicates that the western Indian Ocean

110   was much saltier than modern (ED Fig. 1). Hence, the mechanism for glacial Indian

111   Ocean salinification is likely caused by ocean-intrinsic dynamics, rather than

112   atmospheric changes.

113

114   Salinification due to sea level and ITF

115   We find that each Indian Ocean salinification event throughout the last 1.2Ma in the

116   $\delta^{18}O_{sw-ivc}$ stack is induced when global mean sea level (GMSL) falls to around -48m (σ

117   = 19m) with respect to average modern sea level (Figure 2e, f). Repeating the analysis

118   using U1476 $\delta^{18}O_{sw-ivc}$ alone yields nearly the same GMSL threshold of -48m (σ = 17m)

119   (ED Fig. 2). This suggests a systematic link between glacial sea level lowering and the

120   Indian Ocean glacial salinification process. The Indonesian archipelago is characterised

121   as a tectonically stable collection of large shallow seas with modern depths of around

122   50m[18,19], and has been previously highlighted as an area of major land surface re-

123   organisation as a result of changing sea levels[20,21]. During glacial periods, falling GMSL

124   causes a shoaling of water depths in the Indonesian archipelago leading to the

125   resurfacing of land if sea levels decrease further than -50m relative to today. To better

126   characterise changes in the sea-land surface distribution as a result of GMSL variability

127   and subsequent water depth changes, we ran a coupled Sea Level-topography model

128   ANICE-SELEN (ref.[22]; Methods). The model provides global time-step reconstructions

129   of land-vs-sea maps that are based on dynamical reconstructions of global ice sheet

130   change and consideration of glacio-hydro-isostatic processes. This allows us to assess

131   dynamic regional changes in land exposure and flooding and their relationship to

132   GMSL. Our model results show that the greatest changes in sea-to-land surface area

133   across the Indonesian archipelago occur when GMSL is between -2m to -8m, and -42m

134   to -56m (ED Fig. 10). The shallower of these intervals appears to be linked to the initial

135   exposure of shallow marine geomorphological landforms, such as shallow submarine

136   island channels, estuaries, terraces, shore platforms, sand banks, and coral reefs. Its

137   impact on regional circulation and Indian Ocean surface salinity is therefore small. The

138   deeper interval is directly linked to the abrupt exposure of the Java Straits and North

139   Australian continental shelves. The glacial resurfacing of land due to lower GMSL in

140   the Indonesian Archipelago will have important implications for the outflow dynamics

141   of the ITF. Indeed, we find a close correspondence between GMSL and ITF outflow

142   strength, as reconstructed from $\delta^{13}C_{benthic}$ in the Lombok Strait[23] (Figure 2g, h). This

143   suggests that lowering global sea levels causes a reduction in the ITF outflow due to

144   abrupt land surfacing in the Indonesian Archipelago when GMSL falls to -48m relative

145   to today. The Java Straits and North Australian shelves have both been previously

146   hypothesised to influence regional circulation and surface water hydrography[20,23,24].

147   The exposure of North Australian shelves may reduce the outflow profile area, and

148   therefore the outflow volume of the ITF[20,23,24], while the Java Straits influence the

149   salinity and temperature characteristics of the ITF outflow waters that enter the Indian

150   Ocean[23,25]. At times of high sea level stands, open Java Straits allow fresh water lenses

151 from the South China Seas (SCS) to enter the centre of the ITF, causing a hydrographic

152 blockage of surface waters[23]. As a result, the ITF outflow manifests itself as a

153 predominantly thermocline outflow into the Indian Ocean. In contrast, during times

154 of low sea level (GMSL < -48m relative to today), the closure of the Java Straits restricts

155 the inflow of freshwater lenses, reducing the blockage and allowing a surface water

156 driven ITF outflow[23,25]. This is important for ITF hydrography, since tropical surface

157 waters can differ strongly from thermocline waters due to evaporation. As such,

158 surface waters in the ITF will likely be salter and warmer than thermocline waters and

159 will predominantly form the reduced glacial ITF[23,25]. The salinity increase we observe

160 during glaciation in the tropical and subtropical Indian Ocean is therefore likely linked

161 to a large glacial reduction in and slight salinification of the ITF-sourced fresh water

162 entering the Indian Ocean.

163

164 The other important Indian Ocean gateway

165 In the south west, the Agulhas Leakage (AL) provides a link between the Indian and

166 Atlantic Oceans. Changes in the AL strength can also influence surface hydrography in

167 the Indian and Atlantic Ocean (e.g. refs.[26,27]). AL strength reconstructions suggest that

168 its volume transport and/or surface temperature and salinity was reduced during

169 glacials within the last 500kyr[28,29] (Figure 2i-j). This could be linked to northward shifts

170 of the super gyre boundary or the dynamical subtropical front, coupled to changes in

171 Southern Ocean dynamics, which diminish the outflow space for warm and salty

172 waters between the subtropical front and the African continent[30,31]. It is possible that

173 a weakened AL could enhance the salinification process in the Indian surface Ocean

174 by reducing the outflow of saline waters into the Atlantic and promoting recirculation

175 under net-evaporative conditions in the Indian Ocean. Indeed, published records

176 suggest that the glacial reduction of the AL caused increased recirculation in the

177 southwest Indian Ocean via the Agulhas retroflection, where high evaporation led to

178 salinification of surface waters[26]. However, while Figure 3e and 3i-j show that the

179 increases in $\delta^{18}O_{sw\text{-}ivc}$ were generally initiated during weak AL, in some cycles AL climbs

180 during glacial intensification, while Indian Ocean salinity stays consistently high.

181 Therefore, although the early glacial closure of the AL might have enhanced the initial

182 Indian Ocean salinification process by reducing the outflow of saline waters into the

183 Atlantic, rising AL during glacial intensification would have countered further

184 salinification, and so cannot be the key driving mechanism for the consistent glacial

185 salinification we observe. Instead, we highlight a reduced ITF as the leading driver of

186 glacial Indian Ocean salinification and note that the ITF strength proxy is consistently

187 low during salinification intervals, supporting this idea (Figure 2g).

188

189 A salty Indian Ocean can influence AMOC

190 The high salinity conditions in the glacial Indian Ocean can be traced along the Agulhas

191 current system into the AL in the compiled records (ED Fig. 3c), and thus have the

192 potential to increase salt concentration in the south Atlantic at times when the Indian

193 Ocean is in a salty glacial mode, and the AL is strong. Published AL reconstructions

194 show a resumption of the AL strength at the onset of deglaciations[28,29] (Figure 2i-j),

195 and notable peaks in salinity are seen in the AL region during deglacial Heinrich stadial

196 events[32]. Thus, the high salinity conditions prevalent in the Indian Ocean during glacial

197 maxima would lead to an abrupt release of highly salty waters through enhanced AL

198 during deglaciations, especially in Heinrich stadials, with the potential of influencing

199 downstream salt delivery to the Atlantic meridional overturning circulation (AMOC)

200 (Figure 4). Climate model results investigating the modern AL hint towards an

201 influence of salty Indian Ocean waters on the salinity of the Atlantic, and therefore

202 possibly on AMOC[7]. However, little is known about the impact of a salty AL on the

203 AMOC under glacial conditions. Our data show that the salt-potential of the AL is

204 generally highest during glacial maxima, and would remain high during Heinrich stadial

205 events at the onset of deglaciations, when GMSL is still < -50m relative to today, and

206 the AL strength resumes. We therefore tested the influence of enhanced AL salt

207 import on a suppressed AMOC during a Heinrich stadial using the fully-coupled

208 atmosphere-ocean global circulation model COSMOS[33] (Figure 3; Methods). To

209 simulate this, we first equilibrated the model to LGM conditions (black triangle in

210 Figure 3d). We then performed a classic North Atlantic hosing experiment (LGM015)

211 applying 0.15 Sv for 500 years into the so-called Ruddiman Belt (Figure 3) to generate

212 a weakened AMOC under LGM conditions mimicking a Heinrich stadial (see ref.[33]). To

test the role of an increased AL salt import to the Atlantic, the net result of enhanced deglacial leakage of particularly salty Indian Ocean water, we then conducted two freshwater extraction experiments based on LGM015 by additionally imposing constant high evaporation fluxes over the Agulhas plateau equivalent to 0.05 Sv (LGM015-SA005) and 0.1 Sv (LGM015-SA01) of freshwater extraction. This freshwater extraction occurred while freshwater hosing in the North Atlantic continued. After inducing salinification in the Agulhas plateau area, we see an AMOC recovery in both experiments occurring after ~400 years in LGM015-SA005 and ~250 years in LGM015-SA01, despite the ongoing freshwater hosing (Figure 3). This suggests that enhanced salt import via the AL can have a direct impact on a weakened AMOC and can lead to an AMOC recovery even under a persistent freshwater input in the North Atlantic, which might be expected during deglaciation[8]. Our results further suggest that the elevated amount of salt imported into the South Atlantic has an effect on the response time of the AMOC, with higher salinities leading to faster response times. This underlines that the glacial salinification process in the tropical and subtropical Indian surface Ocean can play an important role for not only the global overturning circulation, but also the shape of deglaciations, depending on the amount of salt harvested throughout the glacial, and the speed of release through the AL. In summary, we highlight the dynamic interplay between different components of the climate system during glacial cycles, showing that falling sea levels during glacial intensification restrict ITF, in turn salinifying the Indian Ocean, which may ultimately trigger abrupt changes in AMOC and shape glacial termination.

MAIN TEXT REFERENCES

1. Sprintall, J., Wijffels, S. E., Molcard, R., & Jaya, I. (2009). Direct estimates of the indonesian throughflow entering the indian ocean: 2004-2006. *Journal of Geophysical Research: Oceans*, *114*(7). https://doi.org/10.1029/2008JC005257

2. Sengupta, D., Bharath Raj, G. N., & Shenoi, S. S. C. (2006). Surface freshwater from Bay of Bengal runoff and Indonesian Throughflow in the tropical Indian

243 Ocean. *Geophysical Research Letters*, *33*(22).

244 https://doi.org/10.1029/2006GL027573

245 3. Talley, L. D., & Sprintall, J. (2005). Deep expression of the Indonesian

246 Throughflow: Indonesian Intermediate Water in the South Equatorial

247 Current. *Journal of Geophysical Research*, *110*(C10), C10009.

248 https://doi.org/10.1029/2004JC002826

249 4. Gordon, A. L., Ma, S., Olson, D. B., Hacker, P., Ffield, A., Talley, L. D., Wilson,

250 D., & Baringer, M. (1997). Advection and diffusion of Indonesian Throughflow

251 Water within the Indian Ocean South Equatorial Current. *Geophysical*

252 *Research Letters*, *24*(21), 2573–2576.

253 https://doi.org/10.1029/97GL01061@10.1002/(ISSN)1944-8007.WOCEEX1

254 5. Durgadoo, J. V., Rühs, S., Biastoch, A., & Böning, C. W. B. (2017). Indian Ocean

255 sources of Agulhas leakage. *Journal of Geophysical Research: Oceans*, *122*(4),

256 3481–3499. https://doi.org/10.1002/2016JC012676

257 6. Beal, L. M., De Ruijter, W. P. M., Biastoch, A., Zahn, R., Cronin, M., Hermes, J.,

258 Lutjeharms, J., Quartly, G., Tozuka, T., Baker-Yeboah, S., Bornman, T.,

259 Cipollini, P., Dijkstra, H., Hall, I., Park, W., Peeters, F., Penven, P.,

260 Ridderinkhof, H., & Zinke, J. (2011). On the role of the Agulhas system in

261 ocean circulation and climate. In *Nature* (Vol. 472, Issue 7344, pp. 429–436).

262 https://doi.org/10.1038/nature09983

263 7. Biastoch, A., Böning, C. W., Schwarzkopf, F. U., & Lutjeharms, J. R. E. (2009).

264 Increase in Agulhas leakage due to poleward shift of Southern Hemisphere

265 westerlies. *Nature*, *462*(7272), 495–498.

266 https://doi.org/10.1038/nature08519

267 8. Knorr, G., & Lohmann, G. (2003). Southern ocean origin for the resumption of

268 Atlantic thermohaline circulation during deglaciation. *Nature*.

269 https://doi.org/10.1038/nature01855

270 9. Gray, W. R., & Evans, D. (2019). Nonthermal Influences on Mg/Ca in

271 Planktonic Foraminifera: A Review of Culture Studies and Application to the

272 Last Glacial Maximum. *Paleoceanography and Paleoclimatology*, *34*(3), 306–

273 315. https://doi.org/10.1029/2018PA003517

10. Kiefer, T., McCave, I. N., & Elderfield, H. (2006). Antarctic control on tropical Indian Ocean sea surface temperature and hydrography. *Geophysical Research Letters*, *33*(24), L24612. https://doi.org/10.1029/2006GL027097

11. Waelbroeck, C., Mulitza, S., Spero, H., Dokken, T., Kiefer, T., & Cortijo, E. (2005). A global compilation of late Holocene planktonic foraminiferal δ18O: relationship between surface water temperature and δ18O. *Quaternary Science Reviews*, *24*(7–9), 853–868. https://doi.org/10.1016/J.QUASCIREV.2003.10.014

12. DiNezio, P. N., Tierney, J. E., Otto-Bliesner, B. L., Timmermann, A., Bhattacharya, T., Rosenbloom, N., & Brady, E. (2018). Glacial changes in tropical climate amplified by the Indian Ocean. *Science Advances*, *4*(12). https://doi.org/10.1126/sciadv.aat9658

13. Thirumalai, K., DiNezio, P. N., Tierney, J. E., Puy, M., & Mohtadi, M. (2019). An El Niño Mode in the Glacial Indian Ocean? *Paleoceanography and Paleoclimatology*, *34*(8), 1316–1327. https://doi.org/10.1029/2019PA003669

14. Clemens, S. C., Yamamoto, M., Thirumalai, K., Giosan, L., Richey, J. N., Nilsson-Kerr, K., Rosenthal, Y., Anand, P., & McGrath, S. M. (2021). Remote and local drivers of Pleistocene South Asian summer monsoon precipitation: A test for future predictions. *Science Advances*, *7*(23), eabg3848. https://doi.org/10.1126/sciadv.abg3848

15. Nilsson-Kerr, K., Anand, P., Sexton, P. F., Leng, M. J., & Naidu, P. D. (2022). Indian Summer Monsoon variability 140–70 thousand years ago based on multi-proxy records from the Bay of Bengal. *Quaternary Science Reviews*, *279*, 107403. https://doi.org/10.1016/J.QUASCIREV.2022.107403

16. Ishikawa, S., & Oda, M. (2007). Reconstruction of Indian monsoon variability over the past 230,000 years: Planktic foraminiferal evidence from the NW Arabian Sea open-ocean upwelling area. *Marine Micropaleontology*, *63*(3–4), 143–154. https://doi.org/10.1016/J.MARMICRO.2006.11.004

17. Kumar K., P., & Ramesh, R. (2017). Revisiting reconstructed Indian monsoon rainfall variations during the last ~25 ka from planktonic foraminiferal δ18O from the Eastern Arabian Sea. *Quaternary International*, *443*, 29–38. https://doi.org/10.1016/J.QUAINT.2016.07.012

306   18. Hanebuth, T. J. J., & Stattegger, K. (2004). Depositional sequences on a late

307   Pleistocene–Holocene tropical siliciclastic shelf (Sunda Shelf, southeast Asia).

308   *Journal of Asian Earth Sciences*, *23*(1), 113–126.

309   https://doi.org/https://doi.org/10.1016/S1367-9120(03)00100-7

310   19. Kudrass, H. R., & Schlüter, H. U. (1994). Development of cassiterite-bearing

311   sediments and their relation to late Pleistocene sea-level changes in the

312   Straits of Malacca. *Marine Geology*, *120*(3), 175–202.

313   https://doi.org/https://doi.org/10.1016/0025-3227(94)90058-2

314   20. Petrick, B., Martínez-García, A., Auer, G., Reuning, L., Auderset, A., Deik, H.,

315   Takayanagi, H., De Vleeschouwer, D., Iryu, Y., & Haug, G. H. (2019). Glacial

316   Indonesian Throughflow weakening across the Mid-Pleistocene Climatic

317   Transition. *Scientific Reports*, *9*(1). https://doi.org/10.1038/s41598-019-

318   53382-0

319   21. Hanebuth, T. J. J., Voris, H. K., Yokoyama, Y., Saito, Y., & Okuno, J. (2011).

320   Formation and fate of sedimentary depocentres on Southeast Asia's Sunda

321   Shelf over the past sea-level cycle and biogeographic implications. *Earth-

322   Science Reviews*, *104*(1), 92–110.

323   https://doi.org/https://doi.org/10.1016/j.earscirev.2010.09.006

324   22. de Boer, B., Stocchi, P., & van de Wal, R. S. W. (2014). A fully coupled 3-D ice-

325   sheet–sea-level model: algorithm and applications. *Geoscientific Model

326   Development*, *7*(5), 2141–2156. https://doi.org/10.5194/gmd-7-2141-2014

327   23. Holbourn, A., Kuhnt, W., & Xu, J. (2011). Indonesian Throughflow variability

328   during the last 140 ka: The timor sea outflow. *Geological Society Special

329   Publication*, *355*, 283–303. https://doi.org/10.1144/SP355.14

330   24. Gordon, A. L., Susanto, R. D., & Vranes, K. (2003). Cool Indonesian

331   throughflow as a consequence of restricted surface layer flow. *Nature*,

332   *425*(6960), 824–828. https://doi.org/10.1038/nature02038

333   25. Sarr, A. C., Husson, L., Sepulchre, P., Pastier, A. M., Pedoja, K., Elliot, M.,

334   Arias-Ruiz, C., Solihuddin, T., Aribowo, S., & Susilohadi. (2019). Subsiding

335   sundaland. *Geology*, *47*(2), 119–122. https://doi.org/10.1130/G45629.1

26. Simon, M. H., Arthur, K. L., Hall, I. R., Peeters, F. J. C., Loveday, B. R., Barker, S., Ziegler, M., & Zahn, R. (2013). Millennial-scale Agulhas Current variability and its implications for salt-leakage through the Indian-Atlantic Ocean Gateway. *Earth and Planetary Science Letters*, *383*, 101–112. https://doi.org/10.1016/j.epsl.2013.09.035

27. Dickson, A. J., Leng, M. J., Maslin, M. A., Sloane, H. J., Green, J., Bendle, J. A., Mcclymont, E. L., Pancost, R. D., Dickson, C. :, Leng, M. J., Maslin, M. A., Sloane, H. J., Green, J., Bendle, J. A., Mcclymont, E. L., & Pancost, R. D. (2010). Atlantic overturning circulation and Agulhas leakage influences on southeast Atlantic upper ocean hydrography during marine isotope stage 11. *Paleoceanography*, *25*(3). https://doi.org/10.1029/2009PA001830

28. Peeters, F. J. C., Acheson, R., Brummer, G. J. A., De Ruijter, W. P. M., Schneider, R. R., Ganssen, G. M., Ufkes, E., & Kroon, D. (2004). Vigorous exchange between the Indian and Atlantic oceans at the end of the past five glacial periods. *Nature*, *430*(7000), 661–665. https://doi.org/10.1038/nature02785

29. Caley, T., Giraudeau, J., Malaizé, B., Rossignol, L., & Pierre, C. (2012). Agulhas leakage as a key process in the modes of Quaternary climate changes. *Proceedings of the National Academy of Sciences of the United States of America*, *109*(18), 6835–6839. https://doi.org/10.1073/pnas.1115545109

30. Bard, E., & Rickaby, R. E. M. (2009). Migration of the subtropical front as a modulator of glacial climate. *Nature*, *460*(7253), 380–383. https://doi.org/10.1038/nature08189

31. De Boer, A. M., Graham, R. M., Thomas, M. D., and Kohfeld, K. E. (2013). The control of the Southern Hemisphere Westerlies on the position of the Subtropical Front. J. Geophys. Res. Oceans, 118, 5669– 5675, https://doi.org/10.1002/jgrc.20407

32. Marino, G., Zahn, R., Ziegler, M., Purcell, C., Knorr, G., Hall, I. R., Ziveri, P., & Elderfield, H. (2013). Agulhas salt-leakage oscillations during abrupt climate changes of the Late Pleistocene. *Paleoceanography*, *28*(3), 599–606. https://doi.org/10.1002/palo.20038

367   33. Zhang, X., Lohmann, G., Knorr, G., & Xu, X. (2013). Different ocean states and

368   transient characteristics in Last Glacial Maximum simulations and

369   implications for deglaciation. *Climate of the Past*, *9*(5), 2319–2333.

370   https://doi.org/10.5194/cp-9-2319-2013

371

372 FIGURE LEGENDS

373 Fig. 1 Geographic and hydrographic context of study sites

374 Modern ocean surface salinity distribution[34] and GEBCO2014 bathymetry[35] plotted

375 using Ocean Data view[36], and orange-to-blue salinity scale, where white represents

376 mean ocean water ~35 psu, with key surface circulation patterns and study sites.

377 Fresher and saltier water mass pathways are indicated with blue and orange arrows,

378 respectively. Location numbers as follows: pink star ④ U1476 (this study); pink circles

379 ① ODP1087[29, 37], ② Agulhas Bank Splice (ABS)[38], ③ MD96-2048[39], ④ U1476 (this

380 study), ⑤ WIND28K[10], ⑥ TY93-929/P[40], ⑦ MD90-0963[41,42], ⑧ GeoB10038-4[43], ⑨

381 MD01-2378[44,45], ⑩ ODP1146[46], ⑪ ODP806[47]. Sites ② – ⑨ are used in our Indian

382 Ocean data stacks. Abbreviations include Agulhas counter current (CC), South China

383 Sea (SCS), Indonesian throughflow (ITF), and west Pacific warm pool (WPWP).

384

385 Fig. 2 Records of Indian Ocean surface salinification and warming compared to

386 changes in Indonesian throughflow and sea level

387 (a) Sea surface temperature (SST) stack (z-scores relative to mean and σ = 1) for the

388 Indian Ocean (bold orange line, from 0 - 790 ka) with upper and lower 95th percentile

389 indicated by orange shaded envelope, and prior to 790 ka, SST data exclusively from

390 U1476 SST (thin orange line; this study). (b), (d) LR04 benthic $\delta^{18}O$[48] with inverted y-

391 axes (grey line). (c), (e) Ice volume-corrected $\delta^{18}O_{sw}$ stack (z-scores) for the Indian

392 surface Ocean (bold green line from 0 – 345 ka) with upper and lower 95th percentile

393 indicated by green shaded envelope, and prior to 345 ka, ice volume-corrected $\delta^{18}O_{sw}$

394 data exclusively from U1476 (thin green line; this study). Green diamonds in (e)

395 indicate the onset of glacial $\delta^{18}O_{sw\text{-}ivc}$ increase within each glacial cycle. (f), (h) global

mean sea level[49] (GMSL, pink line), in (f) with GMSL at onset of $\delta^{18}O_{sw-ivc}$ increases (green diamonds in (e)), horizontal dashed pink line is the average value of all pink circles. (g) Detrended Indonesian throughflow (ITF) outflow strength proxy[23] (blue line). (i) Agulhas Leakage proxy using Agulhas Leakage Fauna (ALF) counts[28] (light grey area). (j) Agulhas Leakage proxy using *G. menardii* counts[29] (dark grey spikes). Intervals of rising $\delta^{18}O_{sw-ivc}$-stack prior to each glacial termination are indicated with vertical grey bars. Glacial terminations are labelled at the top, and indicated with dashed vertical lines.

Fig. 3 Role of intrusion of salinification Indian water mass in deglacial AMOC strength

(a) Sea surface salinity anomaly between the normal LGM background experiment (LGM) which is equivalent to the LGM-W experiment in ref.[33], and the Heinrich-stadial experiment including North Atlantic freshwater hosing (LGM015). (b) and (c) sea surface salinity anomaly between the Heinrich-stadial background setting (experiment LGM015) and anomalies of saltwater hosing experiments equivalent to removal of 0.1 Sv freshwater (LGM015-SA01), and 0.05 Sv freshwater (LGM015-SA005). The average in (b), and (c) respectively, was calculated from the 160th to 210th, and 290th to 340th, model year window. Green and purple rectangles in (a) indicate freshwater hosing and freshwater extraction ("saltwater hosing") in the North and South Atlantic. (d) and (e) time series of AMOC indices and Agulhas Leakage salinity (average in 5° E ~ 20° E and 30° S ~ 40° S). AMOC index from the LGM background climate run (no freshwater hosing), indicated with a black arrow marker (~18 Sv). The AMOC index is defined as the maximum value of the stream function below the water depth of 500 m north of 45° N in the North Atlantic. The map was plotted using the numerical computing environment and programming language Matlab developed by MathWorks. PMIP3 LGM topography/bathymetry were taken from ref[33] according to the PMIP protocol[50].

Fig. 4 Proposed links between sea-level induced changes in the Indonesian throughflow, Indian surface ocean salinity, and efficiency of Agulhas leakage

(a) During interglacials and glaciation, when sea level (SL) is higher than -50 m relative to today, the Indonesian archipelago is submerged leading to a strong Indonesian throughflow (ITF) and import of fresher waters into the Indian Ocean (IO) along the South Equatorial Current (SEC). This coincides with a moderately efficient Agulhas Leakage (AL) south of Africa where the subtropical front (SF) is located further south. (b) During the latter half of the glacial cycle, Indonesian archipelago channels and shallow seas are exposed due to SL lower than -50m relative to today, reducing the ITF and minimising the import of fresher waters into the IO. This coincides with equatorward-shifted glacial SF conditions and a reduced glacial AL. (c) During the onset of deglaciations, the ITF is still reduced because the Indonesian archipelago is still exposed (SL lower than -50m relative to today). However, poleward shift of the SF causes a resumption of the AL which releases highly salty Indian Ocean waters into the South Atlantic. Note all colour bars and patterns are for descriptive purposes only. Top and side panels were plotted using Ocean Data view[36] and bathymetry[35], respectively.

METHODS (2754 words including subheadings)

Age model

The age model for U1476 was taken from ref.[51] who aligned U1476 $\delta^{18}O_{benthic}$ to the $\delta^{18}O_{benthic}$ probability stack[52].

SST and relative salinity derivation

Globigerinoides ruber (*G. ruber*) samples were picked from U1476, then crushed and homogenised. An aliquot of 5 foraminifera was analysed for $\delta^{18}O$ on a MAT253 with a Kiel IV preparation device at Cardiff University. The remaining samples were cleaned and dissolved in a fume hood equipped with HEPA filters under clean laboratory conditions according to ref.[39]. Analysis of Mg/Ca was conducted partially on a Thermo Element XR at Cardiff University, partially on an Agilent Triple Quadrupole at the University of St. Andrews. The instruments were cross-calibrated using the same in-

454 house standard. In both institutions, long term reproducibility of in-house standards

455 yielded RSDs of 1-3 %.

456 SST were calculated from *G. ruber* Mg/Ca using the transfer function and R-script from

457 ref.[9]

458 $$\frac{Mg}{Ca} = e^{0.060(\pm0.008)xT+0.033(\pm0.022)xS-0.83(\pm0.73)x(pH-8)-1.07(\pm0.80)}$$

459 where T is sea surface temperature, S is salinity, and pH is the negative decadic

460 logarithm of H^+ ions. The method[9] allows for the influence of pH and salinity on Mg/Ca,

461 and calculates SST and pH iteratively using Mg/Ca and Antarctic ice core pCO_2[53]. This

462 underlies the assumption that the core site has been at CO_2 equilibrium, or constant

463 disequilibrium throughout the record[9]. Global ocean salinity and alkalinity are

464 calculated from the LR04 benthic $\delta^{18}O$ stack[48] at each time step with modern salinity

465 assumed as 35 psu and modern alkalinity at 2300 µmol/kg[9]. For Late Pleistocene

466 records, pCO_2 can be taken from ice core measurements[53]. Our data exceeds the

467 maximum length of the ice core by several thousand years. We therefore scale the

468 LR04 benthic $\delta^{18}O$ stack[48] to the ice core pCO_2 record[53] (see ED Fig. 2a, b) to provide

469 an estimate of CO_2 change and assign a conservative uncertainty of ±40 µatm (2 σ)[9].

470 SST uncertainties are calculated using Monte-Carlo propagation analysis which

471 accounts for errors on Mg/Ca measurement, SST-equation-calibration errors, salinity

472 errors prescribed as ±1 psu (2 σ), LR04 age model errors prescribed as 4 kyr, alkalinity

473 uncertainty prescribed as -25 to +75 µmol/kg about the modern value using a flat

474 probability distribution[9].

475 Ice volume-corrected seawater $\delta^{18}O$ ($\delta^{18}O_{sw-ivc}$) has been previously used as a proxy for

476 changes in relative seawater salinity in the surface Indian Ocean (e.g. ref.[10]). We

477 therefore correct our $\delta^{18}O_{carbonate}$ according to

478 $\delta^{18}O_{sw-ivc} = \delta^{18}O_{carbonate} - \delta^{18}O_{temperature} - \delta^{18}O_{ice\ volume}$

479 to reflect local $\delta^{18}O_{sw}$ and interpret the results as changes in relative salinity.

480 $\delta^{18}O_{temperature}$ was calculated from Mg/Ca-based temperatures and $\delta^{18}O_{G.\ ruber}$ using the

481 transfer function of ref.[54] for Indian Ocean planktonic foraminifera with a correction

482 factor of +0.20[55]. Analytical errors from $\delta^{18}O_{carbonate}$ and Monte-Carlo-errors from SST

483   were propagated through the calculation. To determine the best correction curve for

484    $\delta^{18}O_{ice\ volume}$ across the last 1.2Ma, we tested the impact of 4 different sea level

485   reconstructions on the resulting $\delta^{18}O_{sw-ivc}$ (ED Fig. 4). Reconstructions of $\delta^{18}O_{ice\ volume}$

486   from ref.[49] based on the LR04 stack[48] gave representative results over the last ~500

487   kyr where different sea level reconstructions can be readily compared and also

488   extends for the ~1.2 Myr duration of our record, and was therefore used to determine

489    $\delta^{18}O_{sw-ivc}$. In Figures 2 and ED Fig. 2, we compare the U1476 $\delta^{18}O_{sw-ivc}$ record to GMSL

490   and the change in land/sea area in the Indonesian archipelago both of which are based

491   on calculations using the U1476 $\delta^{18}O_{benthic}$ record[51]. Using $\delta^{18}O_{ivc}$ from ref.[49] as a

492   correction factor may lead to age model uncertainties when comparing U1476 $\delta^{18}O_{sw-}$

493    $_{ivc}$ to U1476 $\delta^{18}O_{benthic}$[51], and -related results. We therefore also corrected the U1476

494    $\delta^{18}O_{sw-ivc}$ record with $\delta^{18}O_{ivc}$ modelled in ANICE using U1476 $\delta^{18}O_{benthic}$[51]. The resulting

495   age model differences are minimal. For example, when correcting U1476 $\delta^{18}O_{sw}$ with

496   U1476 $\delta^{18}O_{ivc}$, salinification occurs at GMSL of -45 m (σ = 17 m) relative to today which

497   is nearly the same as calculated for the $\delta^{18}O_{sw-ivc}$ stack and U1476 $\delta^{18}O_{sw-ivc}$ corrected

498   using $\delta^{18}O_{ivc}$ from ref.[51].

499   To analyse the lead-lag time between our $\delta^{18}O_{sw-ivc}$, and SST data with $\delta^{18}O_{benthic}$[51], we

500   performed a cross spectral analysis between $\delta^{18}O_{sw-ivc}$, or SST, and $\delta^{18}O_{benthic}$[51]. Both

501   records were first clipped to 1350 ka, then subsampled to 1 kyr. The resulting cross

502   spectral analysis calculated an average lead time of 18 kyr in the $\delta^{18}O_{sw-ivc}$, and 14 kyr

503   in SST to $\delta^{18}O_{benthic}$ at the 95 % confidence interval in the 100-ka periodicity. The

504   phasing results show that both $\delta^{18}O_{sw-ivc}$ and SST lead $\delta^{18}O_{benthic}$ at the 95 % confidence

505   interval.

506

507   SST and $\delta^{18}O_{sw-ivc}$ stack formation

508   The data for the SST and $\delta^{18}O_{sw-ivc}$ stacks was taken from 8 cores spread across the

509   Indian Ocean. We included all cores covering at least the Holocene and LGM at 3 - 4

510   kyr resolution which represent open ocean environments (i.e. to avoid coastal

511   influences), and were able to provide: Mg/Ca- or alkenone-based SST data for the SST

512   stack; Mg/Ca-based SST, and surface foraminifera-based $\delta^{18}O$ for the $\delta^{18}O_{sw-ivc}$ stack.

513   The resulting stacks include the following cores: Agulhas Bank Slice (ABS) (Mg/Ca$_{G.}$

514    $_{bulloides}$, $\delta^{18}O_{G.\ bulloides}$)[38], MD96-2048 (SST$_{Alkenone}$, $\delta^{18}O_{C.\ wuellerstorfi}$)[39], U1476 (Mg/Ca$_{G.\ ruber}$

515   and $\delta^{18}O_{G.ruber}$, this study; $\delta^{18}O_{C.\ wuellerstorfi}$[51]), WIND 28K (Mg/Ca$_{G.\ ruber}$, $\delta^{18}O_{G.\ ruber}$, $\delta^{18}O_{C.}$

516    $_{wuellerstorfi}$)[10], TY93-929/P (Mg/Ca$_{G.\ ruber}$, $\delta^{18}O_{G.\ ruber}$)[40], MD90-0963 (SST$_{Alkenone}$, $\delta^{18}O_{G.}$

517    $_{ruber}$)[41,42], GeoB10038-4 (Mg/Ca$_{G.\ ruber}$, $\delta^{18}O_{G.\ ruber}$, $\delta^{18}O_{C.\ wuellerstorfi}$)[43], and MD01-2378

518   (Mg/Ca$_{G.\ ruber}$, $\delta^{18}O_{G.\ ruber}$)[44,45]. We first re-calculated SST and $\delta^{18}O_{sw\text{-}ivc}$ data from all

519   cores using the same method as described in the methods above for U1476 to ensure

520   methodological consistency. The SST and $\delta^{18}O_{sw\text{-}ivc}$ stacks were then created by

521   splicing the records together and resampling by replacement within a moving 15 kyr

522   window centred on each real data point. The probability of selecting each data point

523   within the window was adjusted using two weights. The first uses a gaussian function

524   (σ = 3 kyr) to weight each point based on its distance from the centre of the window,

525   thus favouring closer data. The second weight is inversely proportional to the relative

526   representation of a given component record within the sampling window, thus acting

527   to mitigate sampling bias. The resampling was performed throughout the spliced

528   record 1000 times to produce a smoothed stack with 95% confidence intervals. Figure

529   2 in the main manuscript shows z-scores of the stacks.

530   We also incorporate age model uncertainties into the stack uncertainty. Because each

531   of the component records used in the stack use a combination of radiocarbon and

532    $\delta^{18}O$ alignment, we take a simple conservative approach and apply a 4 kyr

533   uncertainty[48] to the age models based on the estimated uncertainty for $\delta^{18}O$

534   alignment. This uncertainty was incorporated into the stack by adapting the method

535   of ref.[56], which involves applying an age shift of -2, -1, 0, +1, or +2 kyr (chosen with

536   equal probability) independently to each record during the construction of each of the

537   1000 synthetic records. $\delta^{18}O$ data are shown from each core alongside LR04[48] in ED

538   Fig. 3a and demonstrate a close alignment of age models for these cores on glacial-

539   interglacial timescales.

540

541   Alternative hypothesis testing

542   To test whether the salinification process is also evident in Indian Ocean source waters,

we additionally analysed SST core data from the western Pacific warm pool (ODP806)[47] and the South China Sea (ODP1146)[46] for lead-lag against their respective $\delta^{18}O_{benthic}$ using cross spectral analysis. For the analysis, SST and $\delta^{18}O_{benthic}$ data from the cores was clipped to 6 - 1168 ka, then subsampled at 1 kyr. The cross spectral analysis was conducted between the SST data and their respective $\delta^{18}O_{benthic}$ from the same core using the resampled data. Neither core ODP806[47] or ODP1146[46] showed a significant SST lead at the 95 % confidence interval.

We also used spectral analysis to test whether insolation or monsoon dynamics drive our records. For this purpose, we used U1476, our calculated Indian Ocean surface $\delta^{18}O_{sw-ivc}$ stack, and ocean sediment core U1446 from the Bay of Bengal[14]. We find no significant peak in the precession band for U1476 $\delta^{18}O_{sw-ivc}$ and the Indian Ocean $\delta^{18}O_{sw-ivc}$ stack (ED Fig. 8), and no visual correlation between U1476 $\delta^{18}O_{sw-ivc}$ and 15° S July insolation[57] or African[58], Indian[59] or Southeast Asian[60] monsoonal proxies (ED Fig. 9 c-j). As already pointed out by the authors, there is a significant precession peak for U1446[14] (ED Fig. 8). However, the most significant peak occurs in the 100 kyr periodicity in all records (ED. Figs. 6 - 8). We therefore conclude that insolation and monsoonal changes do not influence U1476 and that the monsoon signal in Indian Ocean salinity records is overprinted by an ice volume signal to different degrees.

ANICE-SELEN sea level-topography model

Simulations of local relative sea level around the Indonesian archipelago were executed using the coupled ice sheet – topography model ANICE-SELEN[22,61]. The 3D ice-sheet model ANICE produces a paleo-GMSL record and, in this study, is forced with U1476 $\delta^{18}O_{benthic}$ data, which acts as a proxy for global ice sheet volume[62,63] while also minimising age model uncertainty in comparisons of model output to our data. Additional inputs of present-day meteorological information, basal and ice sheet height topography for Greenland and Antarctica, and higher resolution topography for currently ice-free Eurasia and North America[61] allow it to solve the ice sheet mass balance for four global ice sheets Greenland, Antarctica, Eurasia, and North America on a 2D grid[61]. This is achieved by decomposing the $\delta^{18}O_{benthic}$ record into its ice

volume and deep-water temperature components using an inverse approach, modelling from the past into the present day[61], where information from the $\delta^{18}O_{benthic}$ data determines the mass balance, and in return mass balance results influence the modelled $\delta^{18}O$. The approach assumes that changes in Northern hemisphere (NH) mid latitude-to-subpolar surface-air temperature anomalies (ΔT_{NH}) are strongly related to changes in ice volume and deep-water formation. Changes in ΔT_{NH} are derived from the difference between modelled $\delta^{18}O$ at time t, and foraminiferal $\delta^{18}O_{benthic}$ at time t + 100 years[61]. Bedrock deformations due to changes in ice volume and resulting influences on GMSL are considered by allowing a downward deflection of the flat elastic lithosphere into a viscous asthenosphere as a result of pressure exerted from above. The SELEN model solves the sea level equation (SLE) accounting for glacial-hydro-isostatic adjustment on a global mesh[22]. In the coupled ANICE-SELEN version, ANICE's ice sheet thickness information, in addition to initial topography information which we assume to be present-day topography in this study, is used to calculate local sea level stands at each GMSL time step as a result of glacial-hydro-isostatic adjustment [22]. Any time lags in isostatic adjustment are accounted for by predicting the effect of sea level change within the next 15 time-steps (around 15 000 years). This information is also returned to ANICE, leading to a more accurate prediction of ice sheet height in the four regional ice sheet models. During times of transient ice sheet height changes, the predicted effect is continuously updated and considers the influence of previous multiple time-steps on the time-step currently calculated[22]. In the end, ANICE-SELEN exports two important variables which involve (i) a reconstruction of GMSL as time transient curve, and (ii) a reconstruction of the local sea level changes as geospatial maps which are made up of land and ocean pixels.

To gain understanding of the land surfacing and flooding rates around the Indonesian archipelago across the Middle to Late Pleistocene (ED Fig. 10), we began running ANICE from t = 1.4 Ma, then started the coupling process at 1.35 Ma with a 100 kyr spin-up period (about 3 glacial cycles) to equilibrate the time-lag in isostatic adjustment. To increase model-run efficiency, we disconnected SELEN after 10 glacial cycles at 0.65 Ma, and ended ANICE modelling at t =0 Ma. We extracted 598 global topography maps from the period between 1250 ka and 651 ka at a temporal

604 resolution of 1 kyr and a spatial resolution of 1 pixel per ~5000 km^2. Each topography

605 map is linked to a period of time, where a GMSL value is calculated from ANICE. Since

606 the tectonics and geomorphology of the Indonesian Archipelago appear relatively

607 constant across the last 1.2 Ma[18,19], we assume that any correlations between changes

608 in the land-ocean ratio and GMSL should also be valid for younger glacial cycles. To

609 calculate changes in above-sea level topography, all maps were processed in Python

610 and cut to the same size, zooming in on the Indonesian archipelago (ED Fig. 10a). Each

611 pixel was given a value of 0, or 1, for ocean, or land, respectively. Then, all pixels of

612 the same value were counted up, and land-to-ocean ratios were calculated for each

613 map as

614
$$R_{land-ocean} = \frac{\sum Pixel_{land}}{\sum Pixel_{ocean}}$$

615 Changes in the land-to-ocean ratio with respect to GMSL [m] were calculated as

616
$$\Delta R_{land-ocean} = \frac{R_{land-ocean}\big(GMSL(t+1)\big) - R_{land-ocean}(GMSL(t))}{GMSL(t+1) - GMSL(t)}$$

617 To identify trends in the sea/land ratio linked to regionally rising and falling sea level,

618 we analysed peaks and troughs in the global mean sea level curve and defined the

619 time between a peak and a trough as "falling", and between a trough and a peak as

620 "rising". The land-ocean ratios corresponding to the different time slices were then

621 sorted into ratios during rising, and ratios during falling GMSL, to understand the

622 dynamics of sea/land changes that occur during rising GMSL and falling GMSL,

623 respectively (see ED Fig. 10).

624

625 Salinity influence on AMOC in COSMOS

626 Four ocean circulation experiments were conducted in the comprehensive climate

627 model COSMOS[33]. These include the LGM (no freshwater hosing) control experiment,

628 the LGM015 (freshwater hosing into the North Atlantic) experiment, the LGM015-

629 SA01 (freshwater extraction in the South Atlantic equivalent to "saltwater hosing" in

630 addition to freshwater hosing in the North Atlantic) experiment, and the LGM015-

631 SA005 (weaker freshwater extraction in the South Atlantic equivalent to "saltwater

632   hosing" in addition to freshwater hosing in the North Atlantic) experiment. Glacial

633   state control settings are taken from the LGM-W experiment from ref.[33] which

634   currently provide the closest match with proxy data We allowed the model to run until

635   the glacial control settings were equilibrated (LGM experiment). Since deglaciations

636   begin with Heinrich events during which the AMOC is strongly suppressed, we

637   perturbed the equilibrium state glacial ocean circulation by imposing a constant 0.15

638   Sv freshwater perturbation over the ice-rafted debris belt in the North Atlantic for 500

639   years (LGM015) (Figure 3) representative of a 10 m/kyr GMSL rise (see also ref.[33]). We

640   then investigated effects of additional salinity perturbations on the Agulhas plateau

641   by removing freshwater from the region through enhanced evaporation. Two salt-

642   water perturbation experiments with evaporation equivalent of the removal of 0.05Sv

643   (LGM015-SA005) and 0.1 Sv (LGM015-SA01) freshwater, representing 1/3 and 2/3 of

644   the freshwater hosing force, were integrated for 800 years based on LGM015 (i.e.

645   under the background climate of persistent freshwater input in the North Atlantic)

646   (Figure 3). In addition, LGM015 is continued for additional 800 years to provide a

647   control run for AMOC changes in LGM015-SA005 and LGM015-SA01. We plot AMOC

648   variability as the AMOC index in Figure 3. Here, we define the AMOC index as the

649   maximum value of the stream function below the water depth of 500m north of 45°

650   N in the North Atlantic in depth-space, effectively representing changes in the rate of

651   North Atlantic deep-water formation and AMOC.

652

653   DATA AVAILABILITY

654   The geochemical datasets produced in this study are freely available at the data

655   repository Pangea.

656

657   CODE AVAILABILITY

658   Python code was used to calculate the stacks, and analyse the ANICE-SELEN image

659   outputs. Both are freely available on Zenodo, for stack calculation

660   (https://zenodo.org/record/7478552; DOI: 10.5281/zenodo.7478552), and ANICE-

661   SELEN image processing (https://zenodo.org/record/7471500; DOI

662   10.5281/zenodo.7471500).

663

664   ADDITIONAL REFERENCES

665   34. Lauvset, S. K., Lange, N., Tanhua, T., Bittig, H. C., Olsen, A. C., Kozyr, A.,

666   Àlvarez, M., Becker, S., Brown, P. J., Carter, B. R., Cotrim da Cunha, L.,

667   Feely, R. A., van Heuven, S., Hoppema, M., Ishii, M., Jeansson, E.,

668   Jutterström, S., Jones, S. D., Karlsen, M. K., Lo Monaco, C., Michaelis, P.,

669   Murata, A., Pérez, F. F., Pfeil, B., Schirnick, C., Steinfeldt, R., Suzuki, T.,

670   Tilbrook, B., Velo, A., Wanninkhof, R., Woosley, R. J., and Key, R. M.

671   (2021). An updated version of the global interior ocean biogeochemical data

672   product, GLODAPv2.2021. *Earth System Sciences Data Discussion, 1-32.*

673   https://doi.org/10.5194/essd-2021-234

674   35. Weatherall, P., Marks, K. M., Jakobsson, M., Schmitt, T., Tani, S., Arndt, J. E.,

675   Rovere, M., Chayes, D., Ferrini, V., & Wigley, R. (2015). A new digital

676   bathymetric model of the world's oceans. *Earth and Space Science*, *2*(8), 331–

677   345. https://doi.org/10.1002/2015EA000107

678   36. Schlitzer, Reiner, Ocean Data View, https://odv.awi.de, 2021

679   37. Pierre, C., Saliège, J. F., Urrutiaguer, M. J., & Giraudeau, J. (2001). *Stable

680   isotope record of benthic and planktonic foraminifera from ODP Site 175-1087

681   in the southern Cape Basin, Atlantic Ocean*. PANGAEA.

682   https://doi.org/10.1594/PANGAEA.701338

683   38. Martinez-Mendez, G., Zahn, R., Hall, I. R., Peeters, F. J. C., Pena, L. D., Cacho,

684   I., & Negre, C. (2010). Contrasting multiproxy reconstructions of surface

685   ocean hydrography in the Agulhas Corridor and implications for the Agulhas

686   Leakage during the last 345,000 years. *Paleoceanography*, *25*(4).

687   https://doi.org/10.1029/2009PA001879

688   39. Caley, T., Kim, J.-H., Malaizé, B., Giraudeau, J., Laepple, T., Caillon, N.,

689   Charlier, K., Rebaubier, H., Rossignol, L., Castañeda, I. S., Schouten, S., &

690   Sinninghe Damsté, J. S. (2011). High-latitude obliquity as a dominant forcing

691   in the Agulhas current system. *Climate of the Past*, *7*(4), 1285–1296.

692   https://doi.org/10.5194/cp-7-1285-2011

693 40. Barker, S., Greaves, M., & Elderfield, H. (2003). A study of cleaning

694   procedures used for foraminiferal Mg/Ca paleothermometry. *Geochemistry,*

695   *Geophysics, Geosystems*, *4*(9), n/a-n/a.

696   https://doi.org/10.1029/2003GC000559

697 41. Rostek, F., Bard, E., Beaufort, L., Sonzogni, C., & Ganssen, G. (1997). Sea

698   surface temperature and productivity records for the last 240 kyr on the

699   Arabian Sea. *Deep-Sea Research Part II: Topical Studies in Oceanography*,

700   *44*(6–7), 1461–1480. https://doi.org/10.1016/S0967-0645(97)00008-8

701 42. Bassinot, F. C., Beaufort, L., Vincent, E., Labeyrie, L. D., Rostek, F., Müller, P.

702   J., Quidelleur, X., & Lancelot, Y. (1994). Coarse fraction fluctuations in pelagic

703   carbonate sediments from the tropical Indian Ocean: A 1500-kyr record of

704   carbonate dissolution. *Paleoceanography*, *9*(4), 579–600.

705   https://doi.org/10.1029/94PA00860

706 43. Mohtadi, M., Lückge, A., Steinke, S., Groeneveld, J., Hebbeln, D., & Westphal,

707   N. (2010). Late Pleistocene surface and thermocline conditions of the eastern

708   tropical Indian Ocean. *Quaternary Science Reviews*, *29*(7), 887–896.

709   https://doi.org/https://doi.org/10.1016/j.quascirev.2009.12.006

710 44. Xu, J., Holbourn, A., Kuhnt, W., Jian, Z., & Kawamura, H. (2008). Changes in

711   the thermocline structure of the Indonesian outflow during Terminations I

712   and II. *Earth and Planetary Science Letters*, *273*(1–2), 152–162.

713   https://doi.org/10.1016/j.epsl.2008.06.029

714 45. Zuraida, R., Holbourn, A., Nürnberg, D., Kuhnt, W., Dürkop, A., & Erichsen, A.

715   (2009). Evidence for Indonesian Throughflow slowdown during Heinrich

716   events 3 to 5. *Paleoceanography*, *24*(2), n/a-n/a.

717   https://doi.org/10.1029/2008PA001653

718 46. Herbert, T. D., Peterson, L. C., Lawrence, K. T., & Liu, Z. (2010). Tropical ocean

719   temperatures over the past 3.5 million years. *Science*, *328*(5985), 1530–1534.

720   https://doi.org/10.1126/science.1185435

721 47. De Garidel-Thoron, T., Rosenthal, Y., Bassinot, F., & Beaufort, L. (2005). Stable

722   sea surface temperatures in the western Pacific warm pool over the past 1.75

723   million years. *Nature*, *433*(7023), 294–298.

724   https://doi.org/10.1038/nature03189

725   48. Lisiecki, L. E., & Raymo, M. E. (2005). A Pliocene-Pleistocene stack of 57

726   globally distributed benthic δ 18O records. *Paleoceanography*.

727   https://doi.org/10.1029/2004PA001071

728   49. de Boer, B., Lourens, L. J., & Van De Wal, R. S. W. (2014). Persistent 400,000-

729   year variability of Antarctic ice volume and the carbon cycle is revealed

730   throughout the Plio-Pleistocene. *Nature Communications*, *5*.

731   https://doi.org/10.1038/ncomms3999

732   50. Braconnot, P., Harrison, S. P., Kageyama, M., Bartlein, P. J., Masson-Delmotte,

733   V., Abe-Ouchi, A., Otto-Bliesner, B., & Zhao, Y. (2012). Evaluation of climate

734   models using palaeoclimatic data. *Nature Climate Change 2012 2:6*, *2*(6),

735   417–424. https://doi.org/10.1038/nclimate1456

736   51. van der Lubbe, H. J. L., Hall, I. R., Barker, S., Hemming, S. R., Baars, T. F., Starr,

737   A., Just, J., Backeberg, B. C., & Joordens, J. C. A. (2021). Indo-Pacific Walker

738   circulation drove Pleistocene African aridification. Nature 598, 618-623.

739   https://doi.org/10.1038/s41586-021-03896-3

740   52. Ahn, S., Khider, D., Lisiecki, L. E., & Lawrence, C. E. (2017). A probabilistic

741   Pliocene–Pleistocene stack of benthic δ18O using a profile hidden Markov

742   model. *Dynamics and Statistics of the Climate System*, *2*(1).

743   https://doi.org/10.1093/climsys/dzx002

744   53. Bereiter, B., Eggleston, S., Schmitt, J., Nehrbass-Ahles, C., Stocker, T. F.,

745   Fischer, H., Kipfstuhl, S., & Chappellaz, J. (2015). Revision of the EPICA Dome

746   C CO 2 record from 800 to 600 kyr before present. *Geophysical Research*

747   *Letters*, *42*(2), 542–549. https://doi.org/10.1002/2014GL061957

748   54. Bouvier-Soumagnac, Y., & Duplessy, J.-C. (1985). Carbon and oxygen isotopic

749   composition of planktonic foraminifera from laboratory culture, plankton

750   tows and Recent sediment; implications for the reconstruction of

751   paleoclimatic conditions and of the global carbon cycle. *Journal of*

752   *Foraminiferal Research*, *15*(4), 302–320.

753   http://dx.doi.org/10.2113/gsjfr.15.4.302

754   55. Pearson, P. N. (2012). Oxygen Isotopes in Foraminifera: Overview and

755   Historical Review. *The Paleontological Society Papers*, *18*, 1–38.

756   https://doi.org/10.1017/s1089332600002539

757   56. Spratt, R. M., & Lisiecki, L. E. (2016). A Late Pleistocene sea level stack.

758   *Climate of the Past*, *12*(4), 1079–1092. https://doi.org/10.5194/cp-12-1079-

759   2016

760   57. Laskar, J., Robutel, P., Joutel, F., Gastineau, M., Correia, A. C. M., & Levrard, B.

761   (2004). A long-term numerical solution for the insolation quantities of the

762   Earth. *Astronomy & Astrophysics*, *428*(1), 261–285.

763   https://doi.org/10.1051/0004-6361:20041335

764   58. Johnson, T. C., Werne, J. P., Brown, E. T., Abbott, A., Berke, M., Steinman, B.

765   A., Halbur, J., Contreras, S., Grosshuesch, S., Deino, A., Scholz, C. A., Lyons, R.

766   P., Schouten, S., & Damsté, J. S. S. (2016). A progressively wetter climate in

767   southern East Africa over the past 1.3 million years. *Nature*, *537*(7619), 220–

768   224. https://doi.org/10.1038/nature19065

769   59. Kathayat, G., Cheng, H., Sinha, A., Spötl, C., Edwards, R. L., Zhang, H., Li, X., Yi,

770   L., Ning, Y., Cai, Y., Lui, W. L., & Breitenbach, S. F. M. (2016). Indian monsoon

771   variability on millennial-orbital timescales. *Scientific Reports*, *6*(1), 24374.

772   https://doi.org/10.1038/srep24374

773   60. Cheng, H., Edwards, R. L., Sinha, A., Spötl, C., Yi, L., Chen, S., Kelly, M.,

774   Kathayat, G., Wang, X., Li, X., Kong, X., Wang, Y., Ning, Y., & Zhang, H. (2016).

775   The Asian monsoon over the past 640,000 years and ice age terminations.

776   *Nature*, *534*(7609), 640–646. https://doi.org/10.1038/nature18591

777   61. de Boer, B., van de Wal, R. S. W., Lourens, L. J., Bintanja, R., & Reerink, T. J.

778   (2013). A continuous simulation of global ice volume over the past 1 million

779   years with 3-D ice-sheet models. *Climate Dynamics*, *41*(5), 1365–1384.

780   https://doi.org/10.1007/s00382-012-1562-2

781   62. Elderfield, H., Ferretti, P., Greaves, M., Crowhurst, S., McCave, I. N., Hodell,

782   D., & Piotrowski, A. M. (2012). Evolution of ocean temperature and ice

783   volume through the mid-Pleistocene climate transition. *Science*, *337*(6095),

784   704–709. https://doi.org/10.1126/SCIENCE.1221294/

785   63. Shackleton, N. J. (1987). Oxygen isotopes, ice volume and sea level.

786   *Quaternary Science Reviews*, *6*(3–4), 183–190. https://doi.org/10.1016/0277-

787   3791(87)90003-5

788   64. Grant, K. M., Rohling, E. J., Bronk Ramsey, C., Cheng, H., Edwards, R. L.,

789   Florindo, F., Heslop, D., Marra, F., Roberts, A. P., Tamisiea, M. E., & Williams,

790   F. (2014). Sea-level variability over five glacial cycles. *Nature Communications*

791   *2014 5:1*, *5*(1), 1–9. https://doi.org/10.1038/ncomms6076

792   65. Wang, P., Tian, J., & Lourens, L. J. (2010). Obscuring of long eccentricity

793   cyclicity in Pleistocene oceanic carbon isotope records. *Earth and Planetary*

794   *Science Letters*, *290*(3–4), 319–330.

795   66. U.K. Met Office (2010). Cartopy: A cartographic python library with a

796   matplotlib interface. *Exeter, Devon*.

797   67. Natural Earth (2015). Free vector and raster map data. Available at

798   www.naturalearthdata.com

799

813

814 AUTHOR CONTRIBUTIONS

815 S.N. collected, analysed and interpreted the data. S.N. wrote the paper, with support

816 from all co-authors. J.W.B.R., M.B.A., and S.B. supported the collection, analysis, and

817   interpretation of the data, and provided the grant. X.Z. and Y.S. conducted the GCM

818   model simulations and supported the interpretation of the results. M.D.D. computed

819   the data stacks and supported the interpretation of the results. B.dB. and H.T.M.

820   conducted model runs and postprocessing of sea level and land/sea ratio

821   reconstructions and supported the interpretation of the results. The samples were

822   collected by S.B. and I.R.H on IODP expedition 361. All authors provided comments on

823   the final manuscript.

824

825   AUTHOR INFORMATION

826   *Competing interests*

827   The authors declare no competing interests.

828

829   *Corresponding author*

830   Correspondence to Sophie Nuber (snuber@ntu.edu.tw)

831

832   EXTENDED DATA LEGENDS

833   <u>Extended Data Fig. 1 U1476 sea surface hydrography reconstructions in comparison</u>

834   <u>to U1476 benthic oxygen isotopes</u>

835   (a), (c), and (f) benthic foraminifera $\delta^{18}O^{51}$ on inverted y-axes (light blue lines), (b)

836   planktonic $\delta^{18}O_{carbonate}$ from *G. ruber* on inverted y-axis (green line; this study), (d)

837   planktonic Mg/Ca with log-scale y-axis and (e) calculated SSTs (red line; this study)

838   with Monte-Carlo propagated errors including analysis, age model, and equation

839   calibration errors plotted as red shaded envelope, (g) calculated ice-volume corrected

840    $\delta^{18}O_{sw-ivc}$ for the surface ocean as proxy for salinity, derived from the $\delta^{18}O_{G.\ ruber}$ and

841   SST records (dark green; this study) with propagated errors including Monte-Carlo SST-,

842   and $\delta^{18}O_{G.\ ruber}$ -analysis errors plotted as dark green shaded envelope. The centre of

843   each deglaciation is indicated by dashed vertical lines and labelled T1 to T16. Note the

844   increases in SST and $\delta^{18}O_{sw-ivc}$ during glacial periods (grey shaded bars).

845

846 <u>Extended Data Fig. 2 Derivation and alternative derivations of the newly presented</u>

847 <u>climate proxies</u>

848 (a) Atmospheric CO_2 from Antarctic ice cores[53] (pink) and calculated using linear

849 transfer from the LR04 benthic $\delta^{18}O$ stack[48] (dark red), which is plotted in (b). (c)

850 Resulting SST calculations using the method of ref.[9] with ice core CO_2[53] (pink), and

851 LR04[48]-based CO_2 (dark red). (d) Difference between $\delta^{18}O$ of global ice volume[49] (blue)

852 and U1476 seawater (this study) prior to the ice volume correction (green). The large

853 difference suggests that there is a substantial local salinity signal which cannot be

854 explained by whole ocean changes. (e) Age model comparison using benthic $\delta^{18}O$ for

855 all sites in Fig. 2 (this study and refs[23,28,29]). (f) U1476 salinity proxy (dark green; this

856 study); dark green diamonds highlight times of salinification onset, and (g) GMSL[49]

857 (pink) highlighting sea level stands at times of salinification onset in pink dots. The

858 analysis corresponds to Fig. 2e, f, and results in the same average GMSL stand (dashed

859 pink line) at which salinification occurs. Deglaciations are plotted as dashed vertical

860 lines, and intervals of rising $\delta^{18}O_{sw\text{-}ivc}$ prior to each glacial termination are indicated

861 with vertical grey bars. Note y-axes in (b), (d), and (e) are inverted.

862

863 <u>Extended Data Fig. 3 Indian Ocean salinity and temperature stack construction</u>

864 (a) Age model comparison using benthic $\delta^{18}O$ for all cores included in the stacks on an

865 inverted y-axis. The colours of the labels correspond to the coloured lines in all panels.

866 References for all cores are listed in Figure 1 and Methods. (b) All SST records which

867 are included in the SST stack. (c) All salinity proxy records which are included in the

868 salinity stack. (d) z-scores of all SST records included in the SST stack, the SST stack

869 (thick black line) with 95th percentile error envelope (grey shaded band), and an SST

870 stack excluding U1476 data with 95th percentile envelope (orange shaded band). (e) z-

871 scores of all salinity proxy records included in the salinity stack, the salinity stack (thick

872 black line) with 95th percentile error envelope (grey shaded band), and a salinity stack

873 excluding U1476 data with 95th percentile envelope (orange shaded band). Note that

874 there is no difference in the onset of the salinification and warming between the black

875   and orange stacks suggesting that U1476 does not force the stack calculations.

876   Intervals of rising $\delta^{18}O_{sw-ivc}$ prior to each glacial termination are indicated with vertical

877   grey bars.

878

879   Extended Data Fig. 4 Salinity reconstruction using different global mean sea level

880   corrections

881   (a) $\delta^{18}O_{sw-ivc}$ records derived using 4 different GMSL reconstructions for the ice volume

882   correction. U1476 $\delta^{18}O_{benthic}$[51] is plotted in b) for lead-lag comparison. Grey bars

883   highlight the early increase in $\delta^{18}O_{sw-ivc}$ prior to terminations. The ref.[49] ice volume

884   correction allowed modelled ice volume $\delta^{18}O$ to be used (dark green). For other GMSL

885   reconstructions[64,65], a change of 1 % in $\delta^{18}O_{benthic}$ per 120 m GMSL, or maximum

886   reconstructed GMSL was assumed. The colour of each $\delta^{18}O_{sw-ivc}$ record corresponds

887   with the referenced scenario in the other panels. (c) Absolute $\delta^{18}O_{sw-ivc}$ amplitude of

888   the glacial $\delta^{18}O_{sw-ivc}$ maxima compared to the preceding minima for all 4 $\delta^{18}O_{sw-ivc}$

889   scenarios. The colours of the bars correspond to the referenced scenarios in (a). Note

890   that differences between different scenarios are relatively small. (d) Corresponding

891   ice volume $\delta^{18}O$ curves for the 4 GMSL reconstructions. The colours of each line

892   correspond with the referenced scenario in (a). Intervals of rising $\delta^{18}O_{sw-ivc}$ prior to

893   each glacial termination are indicated with vertical grey bars in (a). Note y-axes in (b)

894   and (d) are inverted.

895

896   Extended Data Fig. 5 Surface hydrography in the source regions of the ITF and Indian

897   Ocean

898   (a) U1476 $\delta^{18}O_{sw-ivc}$ (dark green), (b) U1476 Mg/Ca-derived sea surface temperatures

899   (orange) (this study), and (c) U1476 $\delta^{18}O_{benthic}$[51] (thin blue line) from the western

900   Indian Ocean. (d) Alkenone-derived sea surface temperatures (light pink) and (e)

901    $\delta^{18}O_{benthic}$ (thin blue line) from the South China Sea[46]. (f) Mg/Ca-derived sea surface

902   temperatures (brown) and (g) $\delta^{18}O_{benthic}$ (thin blue line) from the western Pacific warm

903   pool[47]. Onset of U1476 glacial salinification highlighted in grey bars. Note that both

904   South China Sea, and western Pacific warm pool records do not show a similarly

905   consistent lead-lag pattern between their respective SST and $\delta^{18}O_{benthic}$ data. Note

906    $\delta^{18}O_{benthic}$ data is presented on inverted y-axes.

907

908   Extended Data Fig. 6 Spectral analysis results for U1476 climate proxies

909   Spectral analysis of U1476 SST (a), $\delta^{18}O_{sw-ivc}$ (b), and $\delta^{18}O_{benthic}$[51] (c); as well as SST z-

910   score stack (e), $\delta^{18}O_{sw-ivc}$ z-score stack (f), and LR04 $\delta^{18}O_{benthic}$ stack for comparison (g).

911   Peaks above the red line are significant at the 95% interval. Black dashed vertical lines

912   indicate precession (23 kyr), obliquity (41 kyr), and eccentricity (100 kyr) periodicities.

913

914   Extended Data Fig. 7 Cross spectral analysis results for U1476 climate proxies showing

915   lead-lag characteristics

916   Cross spectral analyses showing coherence (red) and phase (black) between U1476

917   SST, $\delta^{18}O_{sw-ivc}$, and $\delta^{18}O_{benthic}$[51] (top, a-c); and SST stack, $\delta^{18}O_{sw-ivc}$ stack, and LR04

918    $\delta^{18}O_{benthic}$ stack[48] (bottom, d-f). Coherence data above the red, and purple, line

919   indicates significant coherence between datasets at the 95 %, and 80 %, significance

920   level. Phase data at times of significant coherence above the black line (Phase = 0)

921   indicate significant lead of the first variable. Precession (23 kyr), obliquity (41 kyr), and

922   eccentricity (100 kyr) periodicities are indicated by vertical black dashed lines.

923

924   Extended Data Fig. 8 Spectral and cross-spectral analysis results for previously

925   published hydrography data from U1446 in the Bay of Bengal

926   (a) Spectral analysis of $\delta^{18}O_{benthic}$, and (b) $\delta^{18}O_{sw-ivc}$. (c) Phase and coherence between

927    $\delta^{18}O_{benthic}$ and $\delta^{18}O_{sw-ivc}$. Black horizontal line shows Phase = 0; positive/negative phase

928   values indicate 1st variable/2nd variable in the header leading the other variable.

929   Vertical brown line indicates coherence 95% confidence interval. Precession (23kyr),

930   obliquity (41kyr), and eccentricity (100kyr) periodicities are indicated by vertical black

931   dashed lines. All data that went into this analysis was previously published in (ref)[14].

932

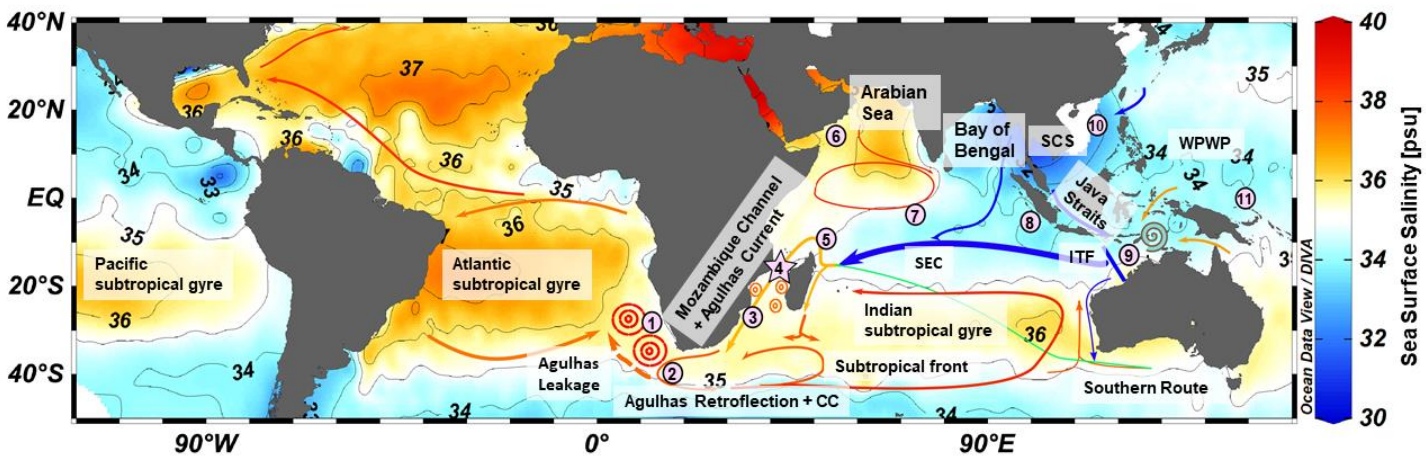933   Extended Data Fig. 9 Indian Ocean hydroclimate proxies compared to U1476 salinity

934   (a) 15° S July summer insolation[57]. (b) – (d), (f), (h), (j), (l), (n), (p) U1476 $\delta^{18}O_{sw\text{-}ivc}$ (this

935   study). (c) U1476 $\delta^{18}O_{benthic}$[51] on inverted y-axis. (e) Malawi Lake SST, proxy for African

936   Monsoon variability[58]. (g) Speleothem $\delta^{18}O_{CaCO_3}$ from Dongge Cave, China, proxy for

937   Southeast Asian Summer Monsoon variability[60]. (i) Speleothem $\delta^{18}O_{CaCO_3}$ from Bittoo

938   Cave, India, proxy for Indian Summer Monsoon variability[59]. (k) TY93-929/P $\delta^{18}O_{sw\text{-}ivc}$,

939   Arabian Sea surface ocean salinity proxy[40]. (m) U1446 $\delta^{18}O_{sw\text{-}ivc}$, Bay of Bengal sea

940   surface salinity proxy[14]. (o) GeoB10038-4 $\delta^{18}O_{sw\text{-}ivc}$[43], eastern Indian Ocean. Grey

941   vertical bars highlight the period of salinification in U1476 which is also visible in the

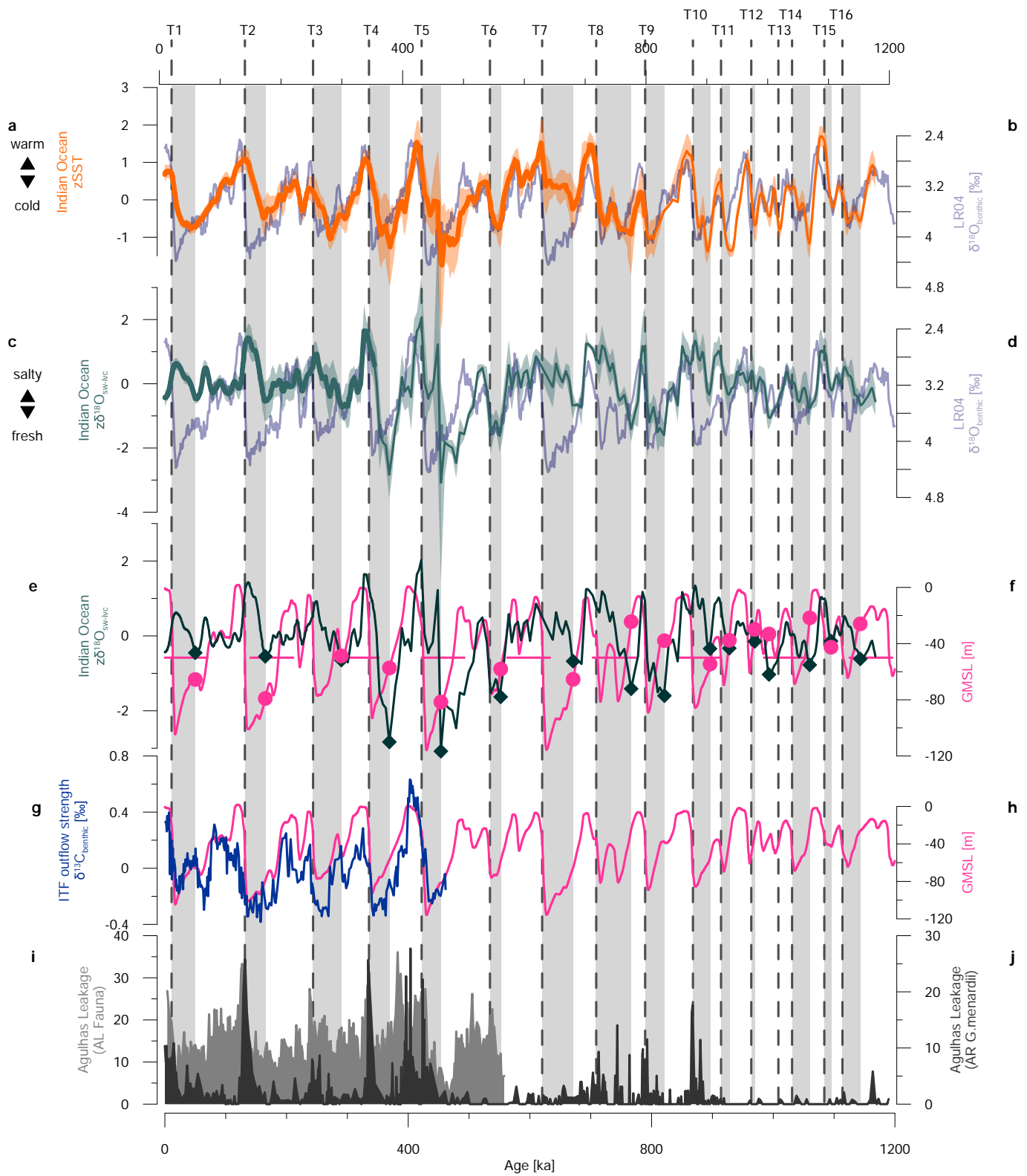942   Arabian Sea, Bay of Bengal, and eastern Indian Ocean sea surface salinity proxies.
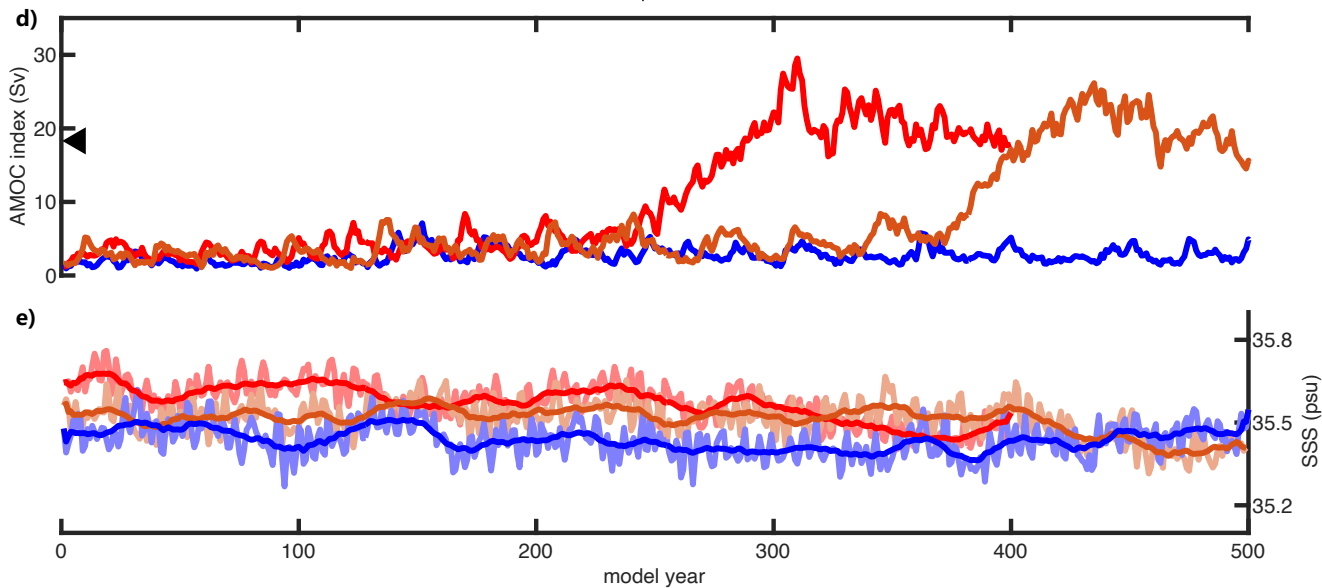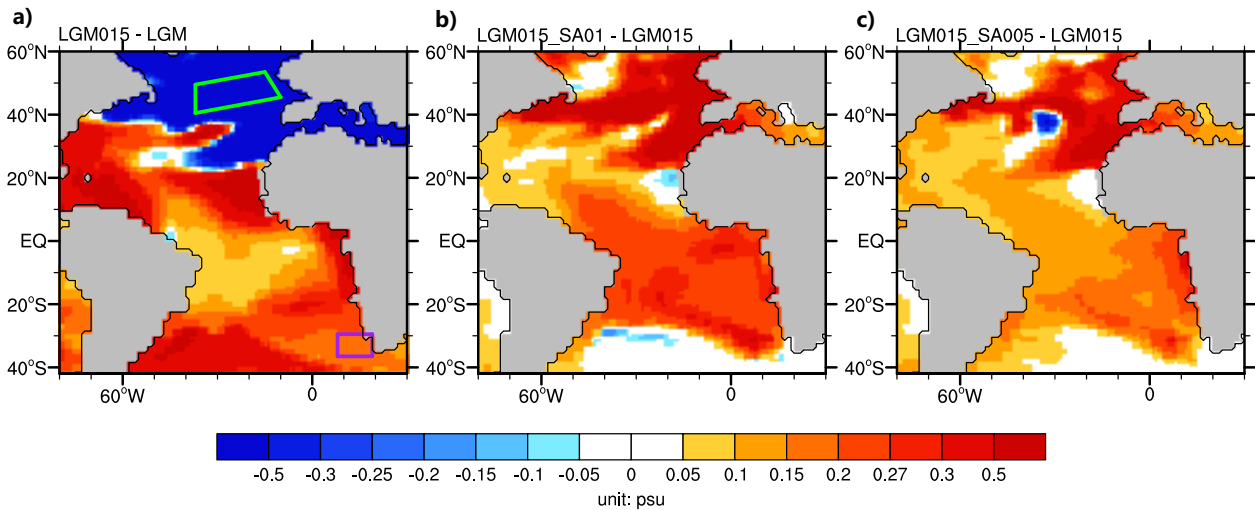
943

944   Extended Data Fig. 10 Changes in land surface as a function of changes in global mean

945   sea level

946   (a) Pixels occurring within the orange polygon were used to calculate the land/sea

947   ratio in each time-slice map created by the ANICE-SELEN model. (b) Change in land to

948   sea surface ratio in the Indonesian archipelago as modelled by the coupled ice sheet-

949   topography model ANICE-SELEN for a subset of 9 glacial-interglacial cycles in respect

950   to GMSL. Changes occurring from falling and rising sea level are plotted in blue and

951   orange respectively – the hysteresis between falling and rising sea levels results from

952   the delayed response of the solid Earth to changes in ocean water surface loading. (c)

953   Slope of the land/sea surface ratio as a function of GMSL to highlight specific sea levels

954   at which the rate of land exposure during sea level fall, or land flooding during sea

955   level rise, is particularly fast with respect to the change in GMSL. Vertical blue shaded

956   bars highlight the GMSL interval within which the change in ratios at GMSL fall is

957   particularly fast. The map in (a) was plotted using the library Cartopy[66] in Python.
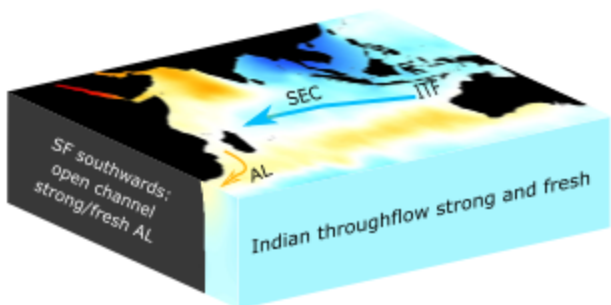
958   Outlines for countries are taken from ref[67].

Indian Ocean surface circulation

a   Glaciation (GMSL drop < 50m)

SEC

ITF

SF southwards:
open channel
strong/fresh AL

AL

Indian throughflow strong and fresh

b   Glacial intensification (GMSL drop > 50m)

SEC

Retroflection

SF northwards:
closed channel
weak/salty AL

Indian throughflow weak and saltier
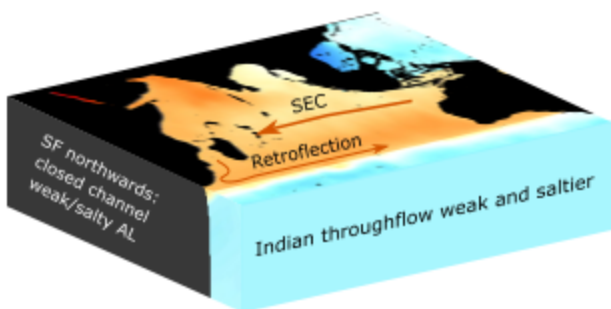
c   Early deglaciation (Heinrich event))

SEC

SF southwards:
open channel
strong/salty AL

AL

Indian throughflow weak and saltier

Schematic Salinity

fresh ◄■■■■■■■■■► salty

a

$\delta^{18}O_{benthic}$

b

SST [°C]

c

$\delta^{18}O_{SW-IVC}$ [‰]

d

zSST

e

$z\delta^{18}O_{SW-IVC}$

Stack
(excluding
U1476)

U1476
ABS
MD96-2048
WIND 28K
TY93-929/P
MD90-0963
GeoB10038-4
MD01-2378

Age [ka]

a δ¹⁸O$_{benthic}$ (U1446)

b δ¹⁸O$_{sw-ivc}$ (U1446)

c δ¹⁸O$_{sw-ivc}$ vs. δ¹⁸O$_{benthic}$ (U1446)

100 kyr   41 kyr   23 kyr

Spectral density

Coherence

Phase [°]

Frequency

Eccentricity   Obliquity   Precession

a

b

c